



UNIVERSITY OF LEEDS

This is a repository copy of *Ductile Deformation Without Localization: Insights From Numerical Modeling*.

White Rose Research Online URL for this paper:
<http://eprints.whiterose.ac.uk/153178/>

Version: Published Version

Article:

Gardner, RL, Piazzolo, S orcid.org/0000-0001-7723-8170, Daczko, NR et al. (1 more author) (2019) Ductile Deformation Without Localization: Insights From Numerical Modeling. *Geochemistry, Geophysics, Geosystems*, 20 (12). pp. 5710-5726. ISSN 1525-2027

<https://doi.org/10.1029/2019GC008633>

©2019. American Geophysical Union. All Rights Reserved. This is an author produced version of a paper published in *Geochemistry, Geophysics, Geosystems*. Uploaded in accordance with the publisher's self-archiving policy.

Reuse

Items deposited in White Rose Research Online are protected by copyright, with all rights reserved unless indicated otherwise. They may be downloaded and/or printed for private study, or other acts as permitted by national copyright laws. The publisher or other rights holders may allow further reproduction and re-use of the full text version. This is indicated by the licence information on the White Rose Research Online record for the item.

Takedown

If you consider content in White Rose Research Online to be in breach of UK law, please notify us by emailing eprints@whiterose.ac.uk including the URL of the record and the reason for the withdrawal request.



eprints@whiterose.ac.uk
<https://eprints.whiterose.ac.uk/>

Geochemistry, Geophysics, Geosystems

RESEARCH ARTICLE

10.1029/2019GC008633

Key Points:

- Areas of distributed strain are either rheologically strong or weak. They can take up significant strain.
- Continuous foliations with no deflection into zones of strain localization cannot be taken as an indicator of a rheologically weak terrain.
- In areas of distributed strain, weakening induced by stress concentration has not occurred.

Supporting Information:

- Supporting Information S1
- Movie S1
- Movie S2

Correspondence to:

R. Gardner,
robyn.gardner@mq.edu.au

Citation:

Gardner, R. L., Piazzolo, S., Daczko, N. R., & Evans, L. (2019). Ductile deformation without localization: Insights from numerical modeling. *Geochemistry, Geophysics, Geosystems*, 20, 5710–5726. <https://doi.org/10.1029/2019GC008633>

Received 20 AUG 2019

Accepted 1 NOV 2019

Accepted article online 11 NOV 2019

Published online 3 DEC 2019

Ductile Deformation Without Localization: Insights From Numerical Modeling

Robyn L. Gardner¹ , Sandra Piazzolo² , Nathan R. Daczko¹ , and Lynn Evans^{1,3} 

¹Australian Research Council Centre of Excellence for Core to Crust Fluid Systems/GEMOC, Department of Earth and Environmental Sciences, Macquarie University, Sydney, New South Wales, Australia, ²School of Earth and Environment, University of Leeds, Leeds, UK, ³School of Earth, Atmosphere and Environmental Sciences, Monash University, Clayton, Victoria, Australia

Abstract Strain is easily localized in a polyphase rock, especially if the rock undergoes syntectonic weakening processes. However, there is ample field evidence for distributed, rather than localized, deformation at the outcrop to hundreds of square kilometer scale. In these areas, distributed strain is evidenced by the presence of continuous foliations and a lack of distinct high-strain zones. Here, we use numerical modeling of viscous deformation to investigate the conditions that allow distributed rather than localized deformation. We identify three strain localization regimes for a system with rheologically strong and weak phases with or without stress-induced weakening. Regime I is characterized by distributed strain. It forms where either deformation-induced interconnection of the weak phase is not possible or the initial weak phase area is intermediate to high (i.e., > ~40–60% of total depending on weak phase geometry). Their resultant bulk strength is either strong or weak, respectively. Regime II is characterized by variably distributed areas of strain localization and develops if the initial proportion of weak phases is intermediate (i.e., 40–60% weak phase depending on geometry) and syntectonic weakening causes an increase (up to ~12%) of weak phase proportion. Regime III exhibits significant strain localization and only develops if the initial proportion of weak phases is relatively low (<20%) and syntectonic weakening increases the proportion of weak phases by over ~12%. Here, high-strain zones readily form irrespective of the initial distribution of rheologically weak and hard phases, and bulk strength is intermediate.

Plain Language Summary Over many years, scientists have concentrated on the question of how deformation is localized in zones of high strain. Hence, areas without these zones, where deformation is distributed, have not been given much attention. This is because it has often been assumed that these areas were insignificant in terms of how deformation is accommodated. In this research we take a different approach and ask the question: “Under what conditions does deformation remain distributed rather than become localized?” To find out, we have run a series of computer simulations testing scenarios that allow or do not allow distributed deformation to occur. If there is a mix of weak and strong phases, for example, two different types of rocks or minerals (as typical in the Earth), then there are two main requirements to form areas of distributed strain: (i) the proportion of weak phases is either high or low (i.e., not intermediate) and (ii) there is no way the strong phase can become weakened. Our results are important for the interpretation of areas that show distributed strain and their significance in the overall deformation of the Earth’s crust and mantle.

1. Introduction

Over the last 50 years, scientists have focused on the mechanisms and conditions of strain localization. High-strain zones (HSZs) are not only easily recognized but arguably focus much of the Earth’s deformation (e.g., Frederiksen & Braun, 2001; Gueydan et al., 2014; Hobbs et al., 1990; Jiang & Williams, 1998; Poirier, 1980; Ramsay, 1980; White et al., 1980). In the upper crust, strain is commonly concentrated into brittle fault zones, while in the middle to lower crust, ductile HSZs dominate (e.g., Ramsay, 1980; Ramsay & Graham, 1970; Sibson, 1977). Consequently, the strain distribution within and around HSZs (e.g., Ramsay, 1980; Ramsay & Graham, 1970), the mechanics of strain localization (e.g., Beach, 1976; Watts & Williams, 1983), the initiation of strain localization (e.g., Mancktelow, 2002; Skemer et al., 2013; Svahnberg &

Piazolo, 2010), and the morphology of HSZs, including the development of mylonites versus ultramylonites and loosely interconnected weak layers (IWL) versus straight, narrow shear zones (e.g., Arbaret et al., 2000; Carreras et al., 2010; Mancktelow, 2002), have all been well studied.

Studies on strain localization show convincingly that strain is readily localized if the rock is polyphase and/or undergoes weakening during deformation. It is also clear that important dynamic feedbacks exist which impact strain localization at the grain scale (Cross et al., 2015; Herwegh et al., 2014; Jessell et al., 2005; Svahnberg & Piazolo, 2010) and/or outcrop and terrain scales (Oliot et al., 2010). Processes enabling strain localization include grain size reduction causing a deformation mechanism change and circulating fluids causing associated growth of rheologically weak phases (e.g., Brodie & Rutter, 1987; Cao et al., 2017; Oliot et al., 2014; Smith et al., 2015 and references therein). Experimental studies show that the presence of a rheologically weak phase and, specifically, the rheological contrast between the weak and strong phases and their distribution has a major impact on strain localization and on the formation and evolution of shear zones (e.g., Dell'Angelo & Tullis, 1996; Gerbi et al., 2016; Shea & Kronenberg, 1993).

This research focus on strain localization contrasts to field studies which show distributed deformation, from outcrop scale to hundreds of kilometer scale, is common. For example, in the now exposed Precambrian shields that consist predominately of middle to lower crustal rocks, extensive, hundreds of kilometer wide areas consist of relatively homogeneous gneissic terrains with continuous regional foliations. Field relationships suggest that no HSZs develop during the initial phase of high-grade deformation (e.g., Nordre Stromfjord, Greenland, Bak et al., 1975; Broken Hill, Australia, Rutland & Etheridge, 1975). During this initial deformation, these terrains are thought to be weak, taking up low levels of strain. The Cretaceous Western Fiordland Orthogneiss, New Zealand, also shows a regional granulite facies foliation marking distributed strain (Clarke et al., 2000). Equally, slate belts which form at midcrustal levels exhibit widespread distributed deformation as they have large areas dominated by a slaty cleavage (e.g., Davis & Forde, 1994 (Fiery Creek slate belt, Australia); Leitch, 1978 (Nambucca slate belt, Australia)). At the same time, geodetic data show that large areas on Earth are currently deforming by distributed strain (e.g., Zheng et al., 2017, India-Eurasia collision zone).

These observations raise the following questions: What strength information can be derived from terrains of distributed strain? What proportion of initial weak phase is needed to sustain distributed but significant strain? Can distributed strain only develop when syntectonic weakening is not occurring?

Here we investigate these questions using a numerical approach. Distributed deformation versus strain localization is monitored throughout the numerical simulations. Two main scenarios are tested: deformation (i) without and (ii) with syntectonic dynamic weakening. Our numerical models show that areas of distributed strain can be either rheologically weak or strong; three aspects are important in their development: (i) operation of syntectonic weakening, and (ii) initial proportion and (iii) geometry of the weak phase.

2. Materials and Methods

2.1. Elle Model

The models use the Elle open source numerical simulation platform (Bons et al., 2008; Piazolo et al., 2018), as developed in Gardner et al. (2017). The models have a 2-D structure with two layers of information. Layer 1 records polygon geometry (Figure 1a and supporting information Figures S1 and S2b), where each polygon has homogeneous viscosity prefactor and viscous flow law, and represents a material domain of similar properties rather than a specific grain. Layer 2 is an initially 100×100 square grid of points (Figure S2b) with material information which act as passive markers of the deformation field as the simulation progresses (e.g., Jessell et al., 2009). Cumulative and instantaneous strain and stress are recorded on both layers at each step of the simulation. The properties are dimensionless, thereby allowing the model to be applicable across all scales.

An Elle control script (Figure S2a) takes the initial geometry and provides the input structure (Figure S2b) to the finite element method code, Basil (Houseman et al., 2008), where the input structure and rheology are deformed with constant displacement of $+0.025$ (top boundary) and -0.025 (bottom boundary) on each step. Dimensionless variables and an incompressible medium behavior (see Text S2 for additional information) are used. The triangulation of the structure for the deformation step preserves the polygon boundaries

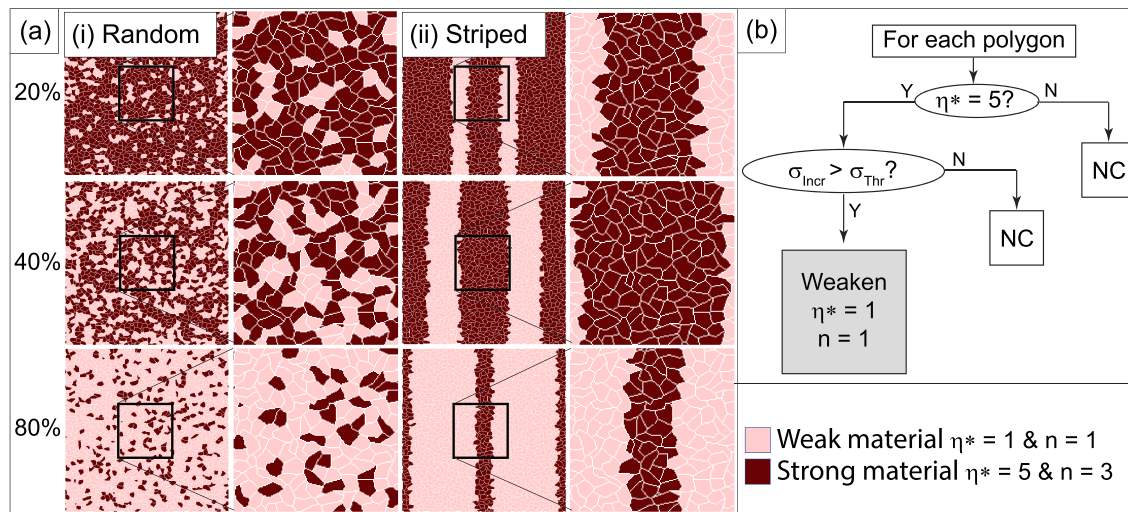


Figure 1. Numerical framework. (a) Selection of geometries for (i) random and (ii) striped geometries at 20, 40, and 80 area% weak phase; center of the geometry (marked) is shown adjacent to the full geometry. All models tested are shown in Figure S1. (b) Schematic diagram showing the logic for stress-induced weakening process; η^* is the viscosity prefactor, n is stress exponent, σ_{Incr} is the incremental stress, σ_{Thr} is the stress threshold, NC signifies no change.

(Figure S3), but the polygon boundaries do not have any inherent localization effect. The model is periodic in both the x and y directions. The Basil solution is used to update the Layer 1 polygon values (e.g., stress and strain) and the Layer 2 node position and values. The weakening process is then optionally called (Figure 1b). This sequence continues until finite shear strain (γ) = 2. Further details are available in supporting information Texts S1 and S2, Houseman et al. (2008), and Gardner et al. (2017).

2.2. Initial Geometry and Rheology

To investigate the effect on strain localization of the initial proportion (area%) of a weak phase, geometries with an initial 2, 10, 20, 40, 60, and 80 area% of the weak phase (Figures 1a and S1), that is, from load-bearing framework (LBF) to interconnected weak phase two phase materials (per Handy, 1994) are tested. Since pre-existing structure can influence deformation behavior (e.g., Dell'Angelo & Tullis, 1996; Gardner et al., 2017; Shea & Kronenberg, 1993), we test two end-member geometries: random distribution and vertical stripes. The strong phase has a stress exponent (n) of 3 (non-Newtonian flow) and viscosity prefactor (η^*) of 5 times that of the weak phase which has a stress exponent of 1 (Newtonian flow).

2.3. Implementation of Dynamic Weakening

Studies of shear zone formation have advocated that dynamic weakening throughout the deformation history is a key condition enhancing strain localization (e.g., White et al., 1980). We test the array of initial weak rheology proportions and geometries, with and without dynamic weakening implemented. Approaches to implementing dynamic weakening in numerical models include implementing grain size reduction explicitly (e.g., Cross et al., 2015; Jessell et al., 2005) and implicitly using viscosity as a proxy (e.g., Jessell et al., 2009; Mancktelow, 2002). Rather than defining a particular weakening process, our conceptual model implements stress dependent weakening (Figure 1b) where the viscosity prefactor and stress exponent of a strong Layer 1 polygon ($\eta^* = 5$, $n = 3$) are decreased (to $\eta^* = 1$, $n = 1$) if the incremental stress in the polygon exceeds a specified threshold. This method simulates, for example, stress-induced grain size reduction, which will trigger the transition from dislocation creep to diffusion creep commonly inferred in shear zones (e.g., Barnhoorn et al., 2005; Menegon et al., 2015; Smith et al., 2015; Svahnberg & Piazzolo, 2010). Detailed information on the numerical implementation of the weakening process and physical reasoning for it is provided in Text S3. The stress threshold of 5.5 causes ~4% of polygons to initially weaken in the 10% initial weak phase models (Figure S4).

Table 1

Summary of Models Completed With Results, Including Percentage Change in the Weak Phase Area From the Initial Percentage at $\gamma = 2$ (cf. Figure 5f), Total High-Strain Area at $\gamma = 1$ and 2 (cf. Figures 5a and 5c), Localization Parameter at $\gamma = 2$ (Equation (1), cf. Figure 5g), Bulk Strength at $\gamma = 2$ (cf. Figures 5b and 5d), Type of Deformation (cf. Figure 6), and Which Regime Is Active

Geometry	% Initial weak phase	Weakening process? ($\sigma_{Thr} = 5.5$)	Increase in proportion of weak phase at $\gamma = 2$	% Area high strain at $\gamma = 1$	% Area high strain at $\gamma = 2$	Weak phase parameter (WP) at $\gamma = 2$	Bulk strength at $\gamma = 2$	Distributed deformation SL-IWL or HSZ formed	Regime
Random	2%	No	0	0	0.1	0	4.5	Distributed	I
	10%	No	0	0	0.1	0	4.2	Distributed	I
	20%	No	0	0.3	0.5	0	3.6	Distributed	I
	40%	No	0	0.4	0.3	0	2.7	Distributed	I
	60%	No	0	0.1	0	0	1.6	Distributed	I
	80%	No	0	0	0	0	0.7	Distributed	I
	2%	Yes	19	10.8	12.5	58	2.5	HSZ	III
	10%	Yes	14	8.3	9.0	37	2.6	HSZ	III
	20%	Yes	12	5.4	6.2	20	2.3	HSZ	III
	40%	Yes	4	0.8	0.1	1	2.0	SL-IWL	II
60%	Yes	0	0.1	0	0	1.5	Distributed	I	
80%	Yes	0	0	0	0	0.7	Distributed	I	
Striped	2%	No	0	0	0	0	4.5	Distributed	I
	10%	No	0	0.3	0	0	4.1	Distributed	I
	20%	No	0	0	0	0	3.7	Distributed	I
	40%	No	0	0	0	0	2.8	Distributed	I
	60%	No	0	0	0	0	2.0	Distributed	I
	80%	No	0	0	0	0	0.8	Distributed	I
	2%	Yes	20	6.8	8.8	34	2.5	HSZ	III
	10%	Yes	14	9.5	11.1	46	2.6	HSZ	III
	20%	Yes	15	3.1	6.7	19	2.3	HSZ	III
	40%	Yes	11	0.8	1.6	3	1.8	SL-IWL	II
60%	Yes	5	0.2	0.1	0	1.5	SL-IWL	II	
80%	Yes	0	0	0	0	0.8	Distributed	I	

3. Results

Models of the initial random and striped geometries of 2, 10, 20, 40, 60, and 80 area% weak phase (Figure 1a and S1) are each run without a weakening process and then with a weakening process implemented (Figure 1b). Table 1 lists and summarizes the main features of these models.

3.1. Representation and Analysis Methods of Results

The numerical models presented contain a large array of parameters that can be monitored throughout a single experiment. To support the reader, we provide Table 2 which summarizes the maps and calculations used for the representation and in-depth analysis of results. A set of output examples is included in supporting information Figures S5–S7. In addition to maps derived directly from Elle, we have processed the passive node data in Matlab® (i) to gauge the intensity of local areas of high strain by calculating, at $\gamma = 1$ and 2, the integral of the accumulated strain across the x axis at each y axis value, plotted as a profile parallel to the y axis (Figures 3 and 4, graphs), and (ii) to quantify the area of high strain, where “high-strain” nodes have accumulated strain $>2\gamma$ (used in Figures 5a, 5c, 6b, and 7). As the simulations progress, γ increases thereby causing the “high-strain” threshold to also increase.

To further assess strain localization and its spatial continuity, the neighborhood of each node in the interpolated Layer 2 grid is examined. The number of “high-strain” nodes in the 3×3 local neighborhood based on each node (Figure 6a) in the 99×99 Layer 2 grid is counted (9,801 total nodes; edge nodes are included only as neighbors). Histograms show the number of nodes which have 2 to 9 “high-strain” nodes in the local neighborhood. Most nodes have no “high-strain” neighbors. For the purposes here, we define distributed strain as where no nodes within the 3×3 neighborhood have high strain (2–9 bins = 0). Strain localized

Table 2
Summary Table of Parameters Used to Represent and Analyze Results

Item	Layer Used	Used in	Visualisation	Details
Viscosity	1	Figs. 1a, 2b, S1, S9	Weak phase distribution & SPO	Defined in Elle
Polygon stress	1	Test for weakening		Calculated by Basil & averaged over polygon by Elle
Passive node stress	2	Fig. 2a	Localization of stress	Deformation continuum data calculated by Basil, interpolated onto passive Layer 2 nodes by Elle
Passively deformed mesh	2	Figs. 7, S9, S10, S11	Finite strain evolution	
Incremental strain	2	Fig. S8	Localization of strain	
Accumulated strain	2	Figs. 3, 4, 7, 8		
Area % weak phase & change in area % weak phase	1, Viscosity	Fig. 5e, f	Quantify variation as the model progresses to 2γ	$\Delta \text{area\% weak phase} = (\text{area\% weak phase})_c - (\text{area\% weak phase})_i$
Area % of high strain	2, Accumulated strain	Fig. 5a, c		Area % of the 100x100 grid where nodes are $2x$ the externally imposed shear strain (γ)
Bulk strength	2, Stress	Fig. 5b,d		Total integral of stress over the 100x100 grid at each γ increment.
Profiles of localization intensity at $\gamma = 1$ & 2	2, Accumulated strain	Graphs in Figs. 3, 4, S10, S11	Strain localization intensity	Integral of the local accumulated strain across the 100x100 grid at each Y axis position. Peaks in the graphs show strain localization.
Neighborhood analysis at $\gamma = 2$	2, Accumulated strain	Figs. 6, 7	Quantify the distribution of high strain nodes	The number of "high-strain" nodes in the 3x3 local neighborhood based on each node (Fig. 6a) in the 99x99 grid is counted (9801 total nodes; edge nodes included only as neighbors). Histograms show the number of 2 - 9 "high-strain" nodes in the neighborhood. Most nodes have no "high-strain" neighbors.
Weak phase strain partitioning parameter (WP)	1, Viscosity & 2, Accumulated strain	Fig. 5g	Highlight distributed vs localized strain	$WP = (\text{area \% high strain} / \text{area\% weak phase}) * 100$

Note. Subscripts of i and c are initial and current, respectively.

into IWLs (SL-IWL) is defined as where some 3×3 neighborhoods have "high-strain" nodes, but not all nodes in any neighborhood are high strain (2-8 bins >0 , 9 bin = 0). A HSZ is defined as having 3×3 neighborhoods with all high-strain nodes (9 bin >0).

We use the total integrated stress over the model at each gamma to examine the variation of the bulk strength (S_b) of the material as the simulation progresses (Figures 5b and 5d and Table 2). For all models, the imposed finite strain is the same; hence, this bulk strength is a measure of rheology. That is, rheologically weak bulk behavior is expressed as a low bulk strength which deforms more easily (at lower imposed stress). As bulk strength is directly related to stress, this bulk strength is also a proxy for the energy needed to deform the different geometries.

To highlight distributed versus localized strain a weak phase strain partitioning parameter (WP) is calculated (Figure 5g and Table 2):

$$WP = (\text{area high strain} / \text{area weak phase}) * 100 \quad (1)$$

High WP values mean that much of weak phase areas are also high-strain areas, suggesting appreciable localization into the weak phase. Values close to 0 indicate only a small proportion of weak phase is forming high-strain areas, suggesting homogeneously distributed strain throughout the model and only minor localization.

3.2. General Model Behavior

In general, stress localizes in the strong Layer 1 polygons near the edges of weak phase polygons (Figure 2a, cf. Figure 2b). Furthermore, any SL-IWLs or HSZs form approximately parallel to the shearing direction.

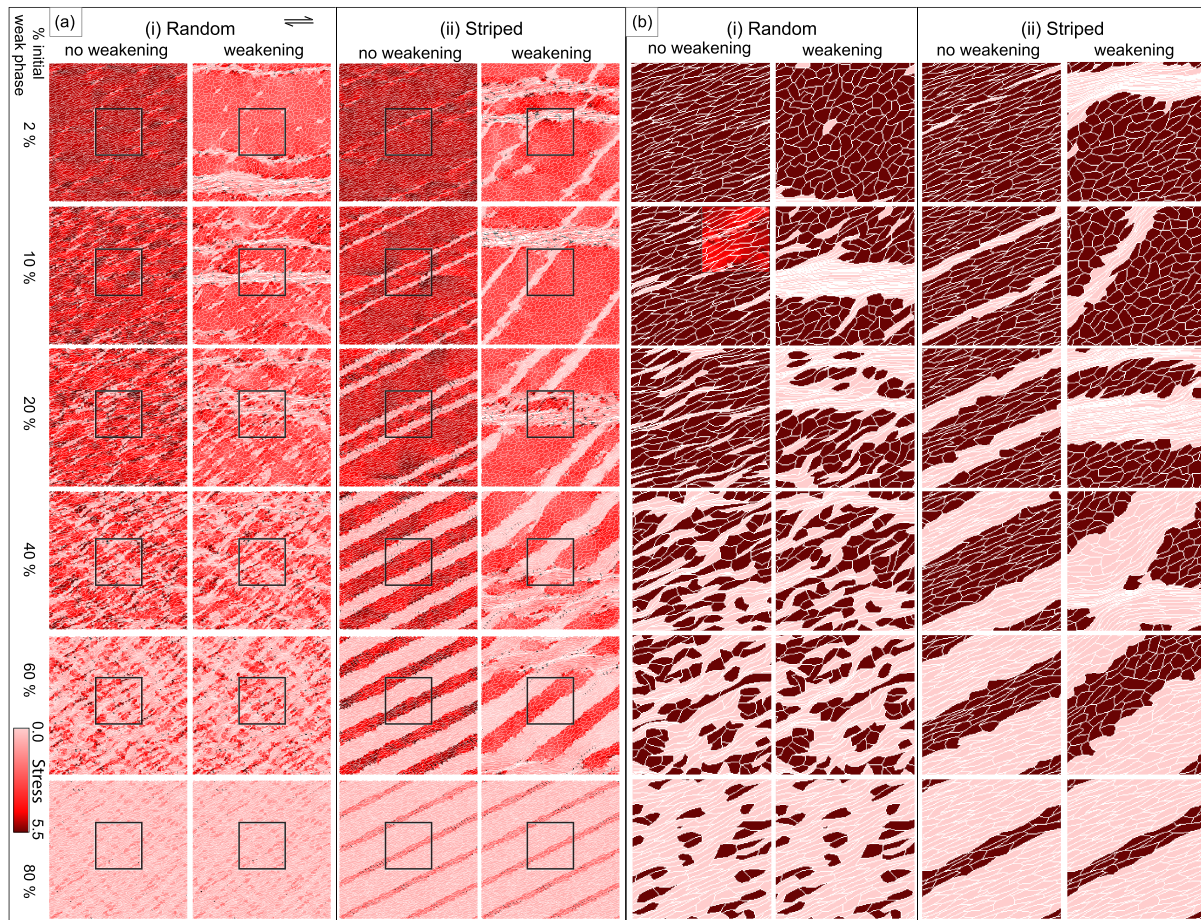


Figure 2. Impact of the weakening process on local stress concentration and local changes in viscosity. (a) Images depict the local stress on the passive node Layer 2 at $\gamma = 2$. (b) Zoom-ins of the center (marked in (a)) of Layer 1 polygon viscosity coefficient for each of the base geometries at $\gamma = 2$; light color depicts rheologically weak polygons; dark color depicts strong polygons; note the change in shape of the initially equiaxial areas. Their shape can be taken as a proxy for the local strain ellipsoid. An overlay of stress in the viscosity zoom image for 10 area% random shows continuous variation of stress across the polygons.

Once formed, strain is concentrated into the SL-IWL or HSZ (Figures 3, 4, and S8) rather than the original weak phase geometry.

At low imposed strain, the proportion of high-strain area is similar for the pairs of models with and without weakening (Figures 5a and 5c), with the 10 area% striped models having the highest proportions of initial high-strain area. The models start to diverge in their behavior where, in models with dynamic weakening, the proportion of weak phase increases (Table 1 and Figure 5e).

The passive distortion of the Layer 2 mesh (Figures 7 and S9–S11) shows the development of strain distribution. The mesh is originally orthogonal; gray lines between Layer 2 nodes were originally vertical, while red lines were originally horizontal. The plots show the gradual convergence of both the red and gray lines in the highly deformed areas where strain is concentrated. In most models, these areas coincide with the Layer 1 weak phase polygons (Figure S9). Strain localization causes the polygons to be elongated in the direction of shearing, resulting in a shape preferred orientation (SPO) subparallel to the shearing direction.

3.2.1. Behavior of Models With No Weakening Process

If dynamic weakening is absent, distributed deformation is observed (Figures 3, S8, and S10) in all striped models irrespective of the initial proportions of weak phases and in random models in the very weak (80 area%) and strong (≤ 20 area%) models. Intermediate random models (40 and 60 area%) have minor interconnection of weak phases. All models with no weakening process have very low or zero area percentages of high strain (Figure 5a and Table 1), causing zero WP values and zero 2–9 bin counts in the node

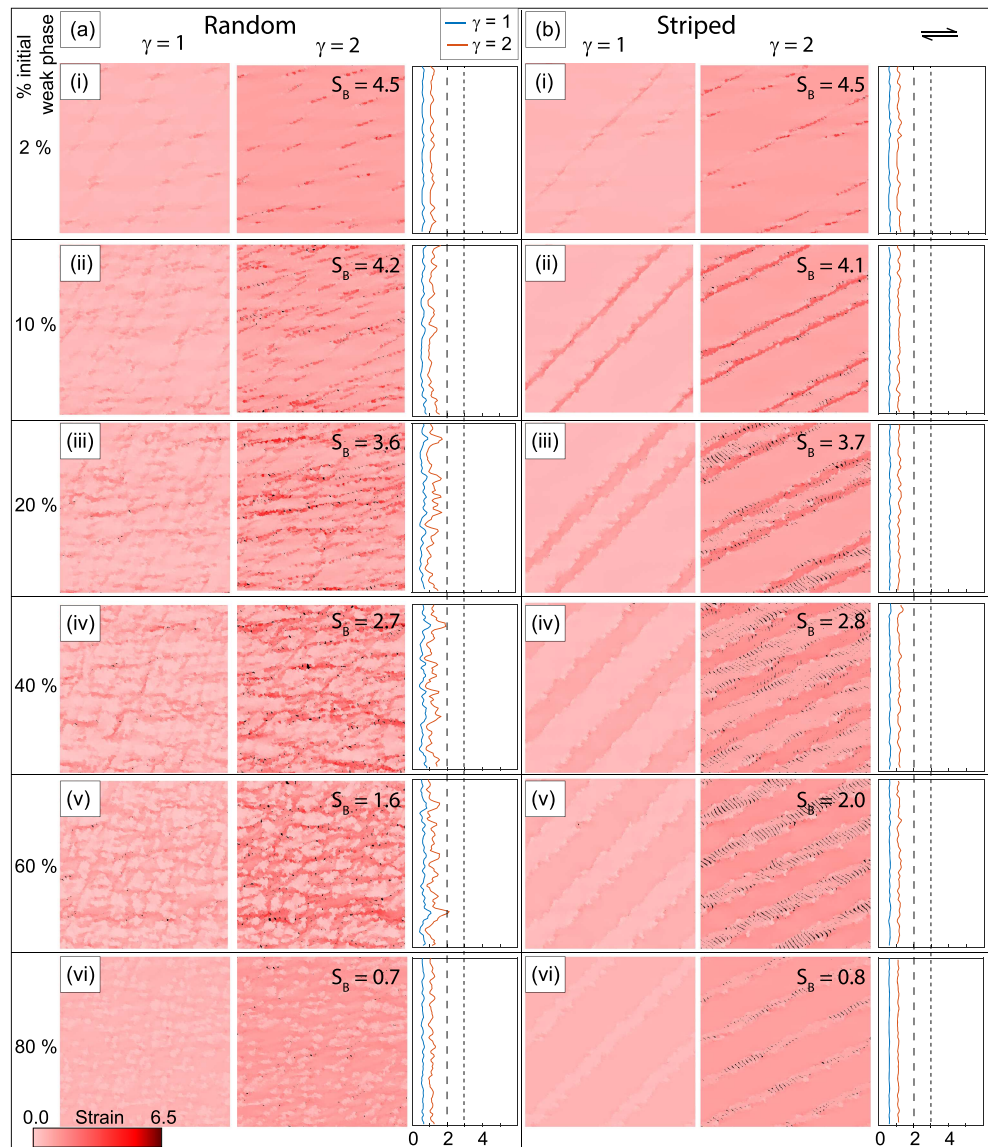


Figure 3. Models without syntectonic weakening; (a) random and (b) striped geometries with variable weak phase (i) 2% through (vi) 80%. Images show accumulated strain on the passively deformed Layer 2 mesh at $\gamma = 1$ and $\gamma = 2$; graphs are profiles of the horizontal bulk strain integral; peaks in the graphs show strain localization intensity; blue $\gamma = 1$ and red $\gamma = 2$; dashed line is cutoff for distributed strain localization, dotted line is cutoff for partial localization, and peaks above dotted line indicate intense localization; S_B is integrated total bulk strain for each model.

neighborhood analysis (Table 1). Bulk strength in the striped model has minor initial variation, while the random models display little to no variation in bulk strength as the deformation progresses (Figure 5b).

Strain distribution across the models (Figure 3) is generally homogeneous with only minor strain heterogeneity observed in the 20–60 area% models. At lower percentages of weak phase (≤ 20 area%), an SPO develops in both the weak and strong phase polygons (Figure 2b). By contrast, in the higher percentage weak phase models (40–80 area%), the strain is concentrated in the weak phase, causing weak phase SPO and only minor strong phase elongation and SPO development.

3.2.2. Behavior of Models With the Weakening Process

If dynamic weakening is implemented and if stress, averaged across the polygon, exceeds the stress threshold of 5.5, the viscosity coefficient and stress exponent of the polygon are reduced. The activity and results of this process are presented in Movies S1 and S2 for the random 10 area% geometry with dynamic weakening.

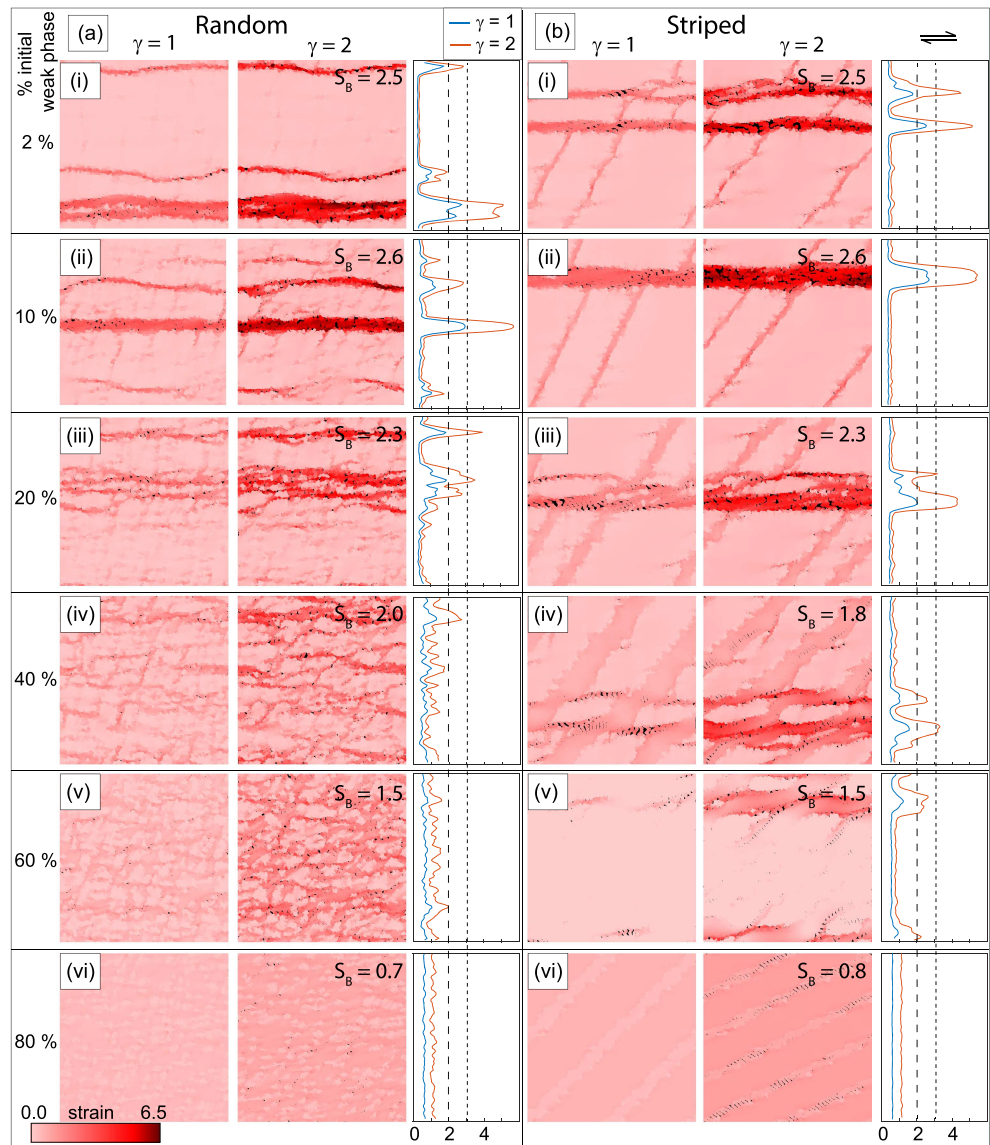


Figure 4. Models with syntectonic weakening; images show accumulated strain on the passively deformed Layer 2 mesh at $\gamma = 1$ and $\gamma = 2$; see Figure 3 for details.

The models show a gradual progression from distributed deformation in the 80 area% models, through partial localization forming SL-IWLs in the 40 and 60 area% models, to concentrated localization with the formation of HSZs in the ≤ 20 area% models (Figures 4, S8, and S11). This is highlighted by the wide variation in area percentages of high strain ($\leq 12.5\%$, Figure 5c and Table 1), WP values (≤ 58 , Figure 5g and Table 1), and 2–9 bin counts in the node neighborhood analysis (Figure 6b). Bulk strength is variable throughout each experimental run. This variation is not always systematic as strain increases but can fluctuate, particularly in the models with low initial weak phase proportions (≤ 40 area%, Figure 5d and Table 1) where weak polygons interconnect to form SL-IWLs and HSZs. The striped models have minor initial variation (Figure 5d), similar to the models without weakening.

Strain localizes exclusively into the weak phase with a preference to localize into the newly weakened polygons and any interconnected weak areas (SL-IWLs or HSZs), rather than the initial weak polygon geometries (Figures 4, S8, S9, and S11). This behavior is independent of the initial proportions of weak phases and the starting geometry. In contrast to the models with no weakening, at lower percentages of weak phase (≤ 20 area%), SPO develops only in the weak phase.

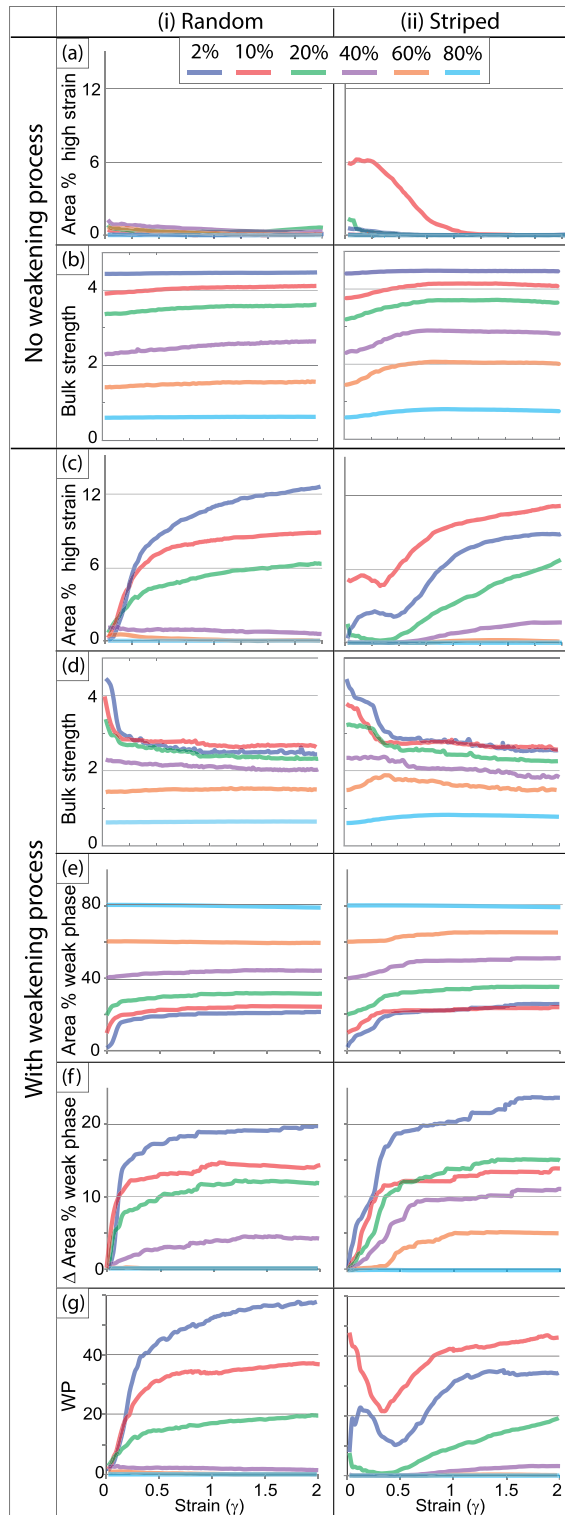


Figure 5. Impact of geometry and initial weak phase area% for models without and with syntectonic weakening; (a and c) percentage of nodes showing high strain (see text for details); (b and d) bulk strength of the model area (see text for details); (e) area percentage of weak phase; (f) change in the area percentage weak phase from the initial area%; (g) localization parameter WP (see text for details); (e, f, and g) shown for models with weakening process only. Values shown are as the imposed strain increases from model initiation to $\gamma = 2$.

3.3. Nature of Strain Distribution

3.3.1. Distributed Strain

An example of the development of distributed strain is provided using the random 60 area% model with weakening implemented (Figure 7a). In this model, the area of high strain is very low at 0.1% at $\gamma = 2$ (Figure 5c(i) and Table 1), and no neighborhoods have >1 high-strain nodes (Figure 7a). The increase in weak phase proportion at $\gamma = 2$ and the WP value are both 0 (Figure 5f and Table 1), and bulk strength does not vary (Figure 5e). Layer 2 mesh strain distribution plots (Figure 7a, right) show minor convergence of the red and gray lines at an angle to the shearing plane as finite strain increases.

Distributed strain is observed in all striped and random models where no weakening was implemented. Where weakening was implemented, both the 60 and 80 area% random models and the 80 area% striped model show distributed strain. All these models have very low or zero values for the area of high strain at $\gamma = 2$ (Figures 5a and 5c and Table 1), zero WP values and zero values for the high-strain neighborhood analysis (Figure 6b, Bins 2–9). They display little evolution, with near steady state bulk strength (Figures 5b and 5d) which varies between the models from very weak (80 area%) to very strong (2 area%). The models where weakening is implemented have bulk strength consistently lower than the models with SL-IWL or HSZ formation.

3.3.2. Partial Localization Including SL-IWL Formation

An example of the development of partial localization is provided using the random 40 area% model with weakening implemented (Figure 7b). In this model, interconnection of weak phases develops (Figure 7b), the area of high strain is low at 0.1% at $\gamma = 2$ (Figure 5c(i) and Table 1) and only a few neighborhoods have high-strain nodes (Figure 7b, Bins 2–3). The increase in weak phase proportion at $\gamma = 2$ is low at 4% (Figure 5f and Table 1), bulk strength varies very little (Figure 5e), and the WP value is low at 1. Layer 2 mesh strain distribution plots show increasing strain concentration with convergence of the red and gray lines at angles close to the shearing plane as finite strain increases.

Where the weakening process was not implemented, the random 40 and 60 area% models display some transitional characteristics between distributed and partial localization with increasing finite strain. Where the weakening process was implemented, both the 40 and 60 area% striped models and the 40 area% random model (Figure 4 and Table 1) display partial localization characteristics. These models have low proportions of high-strain areas at 0.1–1.6 by $\gamma = 2$ (Figure 5c and Table 1), and the high-strain neighborhood analysis shows nonzero values for Bins 2–8 but zero values for the 9 bin (Figure 6b). All show minor weakening (Figure 5e), an increase in weak phase proportion of 4–11% at $\gamma = 2$ (Figure 5f and Table 1), and a minor reduction in bulk strength (Figure 5d). In addition, the models have WP values of ≤ 3 (Figure 5g and Table 1). The bulk strength of the models with partial localization is consistently lower than the models with HSZ formation (Figure 5d and Table 1).

3.3.3. Concentrated Strain Localization With HSZ Formation

Two examples of the development of concentrated strain are provided using the random 10 and 20 area% models with weakening implemented (Figures 7c and 7d). In the 10 area% model, where a narrow HSZ forms, the area of high strain increases steeply to 7.3% by $\gamma = 0.5$ and then

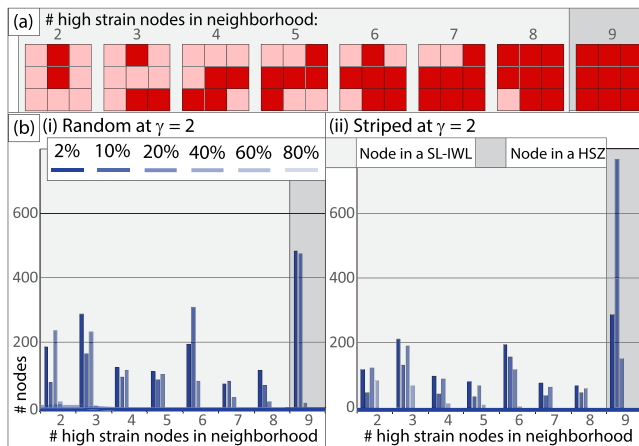


Figure 6. Assessment of Strain Localization; Each 3×3 Block Of Nodes Is checked for the number of nodes with high strain. A histogram is produced of the counted values, only Bins 2–9 shown. Total number of nodes analyzed in each model is 9,801; (a) Examples of the Neighbor Counting On The 3×3 Grids, Examples are 2–9 (As Counted by The Red Squares); (b) Histograms Show Impact Of The (i) Random and (ii) Striped Geometry and Percentage initial weak phase on strain localization at $\gamma = 2$ for models with weakening process. Flat line at 0 is the equivalent for models with no weakening process.

tapers to 9.0% at $\gamma = 2$ (Figure 5c(i) and Table 1). This indicates initiation of localization occurs at low shear strain. This correlates with a sharp increase in weak phase proportion at low strain (Figure 5f, 12.9% by $\gamma = 0.5$), and the neighborhood analysis where the proportion of nodes with all high-strain neighbors is 267 at $\gamma = 0.5$ (Figures 7d and 9 bin). This value increases to 407 at $\gamma = 2$ showing the intensity of strain localization increases with imposed strain. Bulk strength also reduces quickly at low shear strain (Figure 5e) and the WP value is high at 37. The strongly distorted Layer 2 mesh indicates development of concentrated strain where both the original red and gray lines are closely spaced and subparallel to the shearing direction in the HSZ (Figure 7d, right).

By contrast, the second example of HSZ formation (random 20 area%) shows more distributed HSZ formation. Initiation of localization also occurs at low shear strain, but the increase in high-strain area is more gradual from 4.4% by $\gamma = 0.5$ to 6.2% at $\gamma = 2$ (Figure 5c(i) and Table 1). The neighborhood analysis shows a gradual increase in the 5–9 bin counts indicating increasing localization intensity into the HSZ with increasing γ . The 9 bin count varies from 0–14 from $\gamma = 0.5$ –2.0.

Concentrated strain localization does not occur in any models where weakening was not implemented. Where weakening has been implemented, the ≤ 20 area% models for both geometries (Figure 4 and Table 1) display concentrated localization, while the striped 40 area% model has transitional strain characteristics. The models have 6.2–12.5% high-strain

areas by $\gamma = 2$ (Figure 5c and Table 1), and the high-strain neighborhood analysis have significant values for Bins 2–8 and nonzero values for the 9 count (Figure 6b(i)). All show significant weakening, with an increase in the proportion of weak phase (Figure 5e), corresponding to ~ 12 –20% at $\gamma = 2$ (Figure 5f and Table 1), and a reduction in bulk strength (Figure 5d). In addition, the models have high WP values from ~ 19 –58 (Figure 5g and Table 1). The bulk strength of the models with concentrated localization is consistently the highest of the models with weakening (Figure 5d and Table 1).

3.4. Impact of Initial Proportions of the Weak Phase on Stress Concentrations and Associated Strain Localization

The models show that the percentage of initial weak phase has a strong influence on where stress concentrates (Figure 2a) and where weakening processes operate. Hence, it also impacts where strain is localized and whether homogeneous distributed deformation versus SL-IWLs or HSZs develops. Stress concentrates in the strong polygons near a weak polygon (Figures 2a and 2b). As the percentage of initial weak phase increases, the number of weak polygons increases; consequently, the number of strong polygons immediately surrounding those weak polygons also increases. Hence, the stress is distributed over more strong polygons and therefore decreases the stress value within each polygon (Figure 2a). Due to changes in the force chains between strong areas, stress amplification decreases as the proportion of strong phase decreases. At the highest initial percentages of weak phase (all 80 area% models), stress is dispersed over a large area, and therefore the threshold for invoking the weakening process is not reached. In addition, at low initial proportions where HSZs are formed (2, 10 and 20 area%), the HSZs are initiated and localize strain at lower shear strains than for the formation of SL-IWLs (40 area%) (Figures 5c, 5f, and 5g).

As a general guideline, where weakening is allowed, HSZs form at lower initial proportions of weak phase (≤ 10 area%), and as the initial weak phase proportion increases, the HSZs become more dispersed parallel to the shearing direction (20 area%), until these are SL-IWLs (40 area%). As the proportion of initial weak phase increases further, the strain becomes gradually more distributed with the development of distributed deformation lacking SL-IWLs or HSZs, until the strain is homogeneously accommodated (≥ 60 area%).

3.5. Impact of Initial Weak Phase Geometry Relative to Shear Plane

In the striped geometry models with significant interconnection of weak phases (i.e., 10–60 area% models with weakening), the rotation of the weak phase delays the increase in area percentage of weak phase

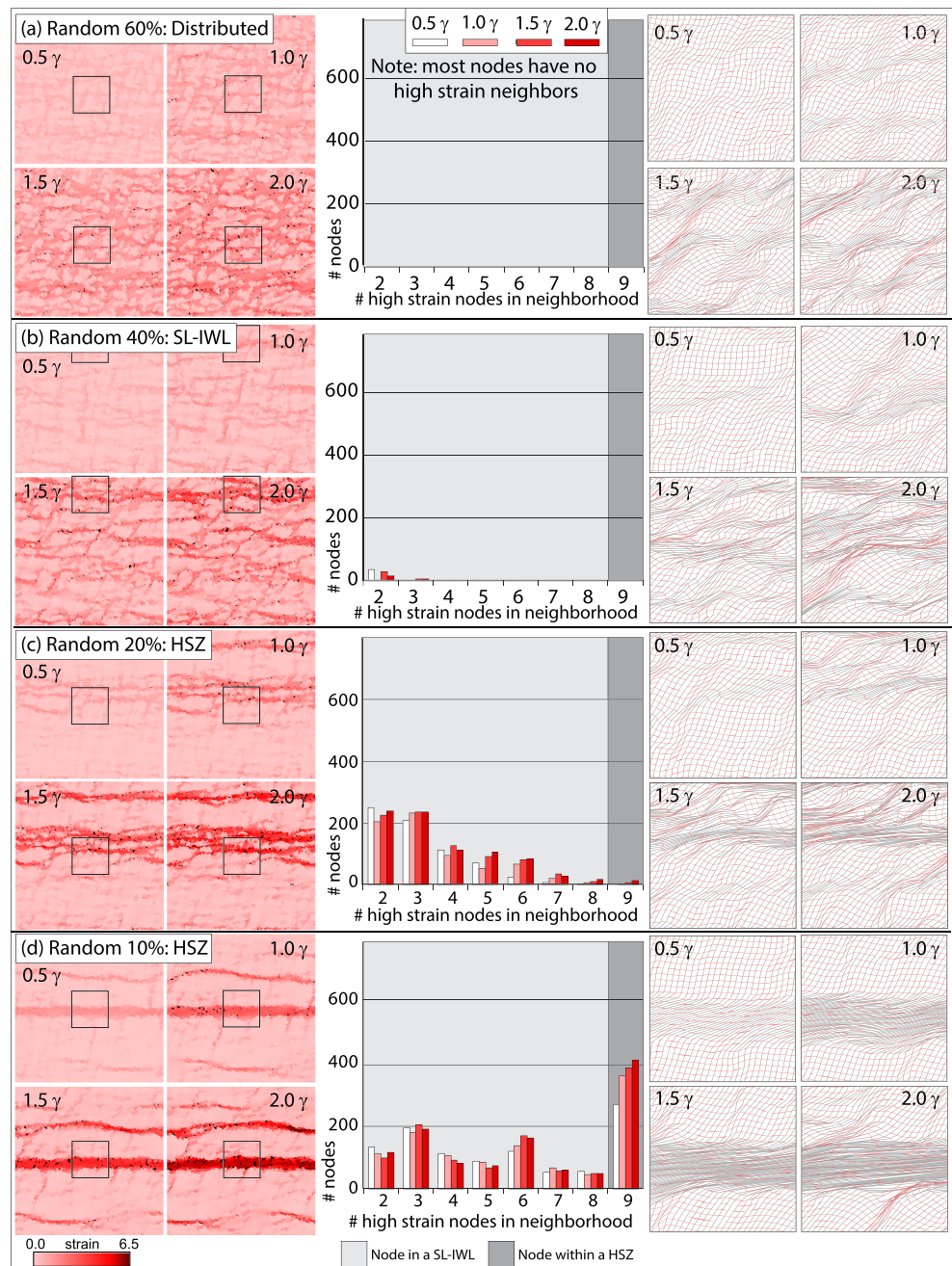


Figure 7. Strain distribution development. Accumulated strain images (left), histograms of high-strain node counts in the 3×3 grid (center), and zoom showing deformation of the passive Layer 2 mesh (right, zoom area marked on left) at $\gamma = 0.5, 1.0, 1.5,$ and 2.0 . (a) Random 60% model, distributed strain; (b) random 40% model, SL-IWL formation; (c) random 20% model transitional SL-IWL to HSZ formation; and (d) random 10% model, HSZ formation.

(Figure 5e(ii)), thereby delaying the reduction in strength (Figure 5d(ii)) and the onset of the strain localization (Figure 5c(ii)), when compared with the random geometry models. In addition, the striped geometry models with no weakening show distributed deformation for all models. By contrast the random models show some interconnection of weak phase and the development of transitional strain characteristics.

Bulk strength is reduced in models with the weakening process implemented due to adding weak phase (Figure 5f), but where HSZs and SL-IWLs form, bulk strength is further reduced by the formation of a shearing parallel (horizontal) weak layer.

4. Discussion

4.1. Relevance of Models to Ductile Deformation Observed in Nature

Our numerical models (and Gardner et al. (2017) are conceptual, as the weakening process and geometries, while being inspired by nature, are generalized and scale independent. The models explore general concepts of distributed strain versus strain localization and quantify the initiation and behavior of strain localization. As such, the principles of pattern formation and strain localization are scale independent and have applicability for geological features at all scales. However, the values provided here should be used only as general guidelines when applying our results to any geological scenarios.

The deformation of the Layer 2 passive mesh (Figures 7 and S9–S11) highlights shearing parallel localization by the closeness of the gray (originally vertical) lines as they rotate into the shear plane. Additionally, the development of SPO in the polygons can be considered equivalent to a foliation formed by rotation of minerals into the shearing direction and/or aligned mineral growth (e.g., Williams, 1976, and references therein). The rotation of the red (originally horizontal) lines away from the shearing plane suggests the formation of other fabrics in the models S-C (e.g. Figure S10, random models without weakening implemented). In the models that form SL-IWL and HSZ, both red and gray lines rotate close to parallel to the shear plane (Figure S11).

4.2. Overview of General Relationships: Regimes of Deformation

Three localization regimes can be distinguished based on heterogeneity and intensity of strain localization at $\gamma = 2$ (Table 3). Each regime is characterized by a specific bulk strength behavior, WP value range (Figure 8), and weak phase area% at $\gamma = 2$.

Regime I is characterized by distributed strain, with very small (<0.1%) area% of high strain; hardly any SL-IWLs or HSZs develop (Figure 7) and peak(s) of the strain integral profile indicate intensity of localization is <2 (Figures 3 and 4). Here, the WP value is 0 and the bulk strength is near steady state. If weakening processes operate, the initial weak phase proportion is >40–60% and additional weakening causes little increase in weak phase area. Where weakening processes do not operate, any proportion of initial weak phase arranged either randomly or in stripes can result in Regime I distributed strain.

In Regime II, SL-IWLs are present and the location, size, and intensity of strain localization changes with increasing strain. It occurs if weakening processes are operating and the initial weak phase proportion is 40–60% with an increase in weak phase of up to ~12%. In addition, the area of high strain <~2%, the WP value is <3 and a minor reduction in the bulk strength occurs. Where weakening processes do not operate, intermediate proportions (40–60 area%) of randomly distributed weak phase can show minor partial localization.

In Regime III, strain is intensely localized into HSZs (see neighborhood analysis, Figure 6), and the peak(s) of the strain integral can reach values >3 (Figure 4). It occurs only if weakening processes are operating and the initial weak phase proportion is <~20% with an increase in weak phase of >12%. In addition, the area of high strain is >~6%, the WP value is >3, and bulk strength reduces with increasing γ .

Regime I with low weak phase area% shows the same stress and strain partitioning characteristics as the LBF rocks of Handy (1994). He suggests IWL microstructures are ubiquitous and rocks with LBF microstructure are rare. We suggest this is because the LBF microstructures will only form in rocks undergoing solid state deformation, where deformation is accommodated by crystal slip without recrystallization. Once weakening commences, by for example, recrystallization to smaller grain sizes or reaction softening, these rocks would be overprinted by HSZs, following the behavior of Regime III.

4.3. Localized, Anastomosing, or Distributed Strain: An Effect of Initial Proportion of Weak Phase and Weakening Potential

In his numerical modeling of a random two phase geometry, Mancktelow (2002) shows that strain softening has an important effect on shear zone development and that where the shear zone propagation is most

Table 3
Summary of Regime Characteristics

Attribute		Regime I	Regime II	Regime III
Strain		Distributed	Partial localization	Concentrated localization
Intensity of localization (Fig. 3 & 4)		0-2	2-3	>3
Weakening process required?		No	Yes	Yes
Area of initial weak phase (with no weakening)		0 - 40% >60%	40 - 60%	N/A
Area of initial weak phase (with weakening)		High (> 60%)	Moderate (40 - 60%)	Low (1 - 40%)
Area percentage high strain at $\gamma = 2$ (Fig. 5a, c, Table 1)	Characteristics	< 0.5%	0.1 - 1.6%	> 1.6%
Increase in proportion of weak phase at $\gamma = 2$ (Fig. 5f, Table 1)		< 4%	4 - 11%	> 11%
Neighbourhood analysis (Fig. 6)		No SL-IWLs or HSZs	SL-IWLs	HSZs
Bulk strength (Fig. 5b, d)		near steady state	minor strength reduction/near steady state	strength reduction
WP value (Table 1)		Very low (< 0.3%)	Intermediate (0.1 - 3.2%)	High (> 3.2%)

Note. Values are relative and indicative only. SL-IWL = strain localizing interconnected weak layer; HSZ = high-strain zone; WP = weakening parameter is a percentage calculated by dividing area of high strain by the area of weak phase.

efficient, the shear zones are straighter and narrower. This observation agrees with our random geometry 2 and 10 area% models with fast development (Figure 5c(i), steepness of graph) of a narrow, straight HSZ (Figure 4a). However, varying the geometry to the striped models causes it to initiate slowly (Figure 4b) but still form a straight and narrow HSZ. This variation in results suggests many aspects, including the initial proportion of weak phase, geometry and weakening potential all impact HSZ development.

The graphs of percentage area of high strain at each step (Figures 5a and 5c) show that the initial increase in weak area proportion per γ is indicative of the efficiency of localization. HSZs have the earliest onset and most efficient localization compared with those models forming SL-IWLs (Figures 5c-5f). This is also reflected in the closer spatial distribution of the high-strain nodes in the HSZs compared with the more spatially distributed, anastomosing character of the SL-IWLs (Figures 4 and 6b).

Our models displaying Regime III have decreasing bulk strength as the SL-IWLs or HSZs form (cf. Figures 5d and 5b). This is partially due to the increase in weak phase proportion (Figures 5e and 5f) but, importantly, is also due to the development of the weak layer parallel to the shearing direction. This horizontal weak layer geometry has been shown to be comparatively the weakest geometry by many experiments both analog (e.g., Dell'Angelo & Tullis, 1996; Holyoke & Tullis, 2006) and numerical (e.g., Cook et al., 2014; Gardner et al., 2017; Gerbi et al., 2015).

4.4. Distributed Deformation in Heterogeneous Rocks

Our models of Regime I show that there are two main possibilities for forming distributed deformation. The first occurs if a terrain is dominated by weak phases. Here, deformation can accommodate high strains without localizing strain into HSZs or SL-IWLs through a dispersed system of interconnected weak phases (Figure 8). However, distributed deformation is also possible in terrains characterized by low levels of weak phase where there is no potential for additional syntectonic weakening of the area. In this case

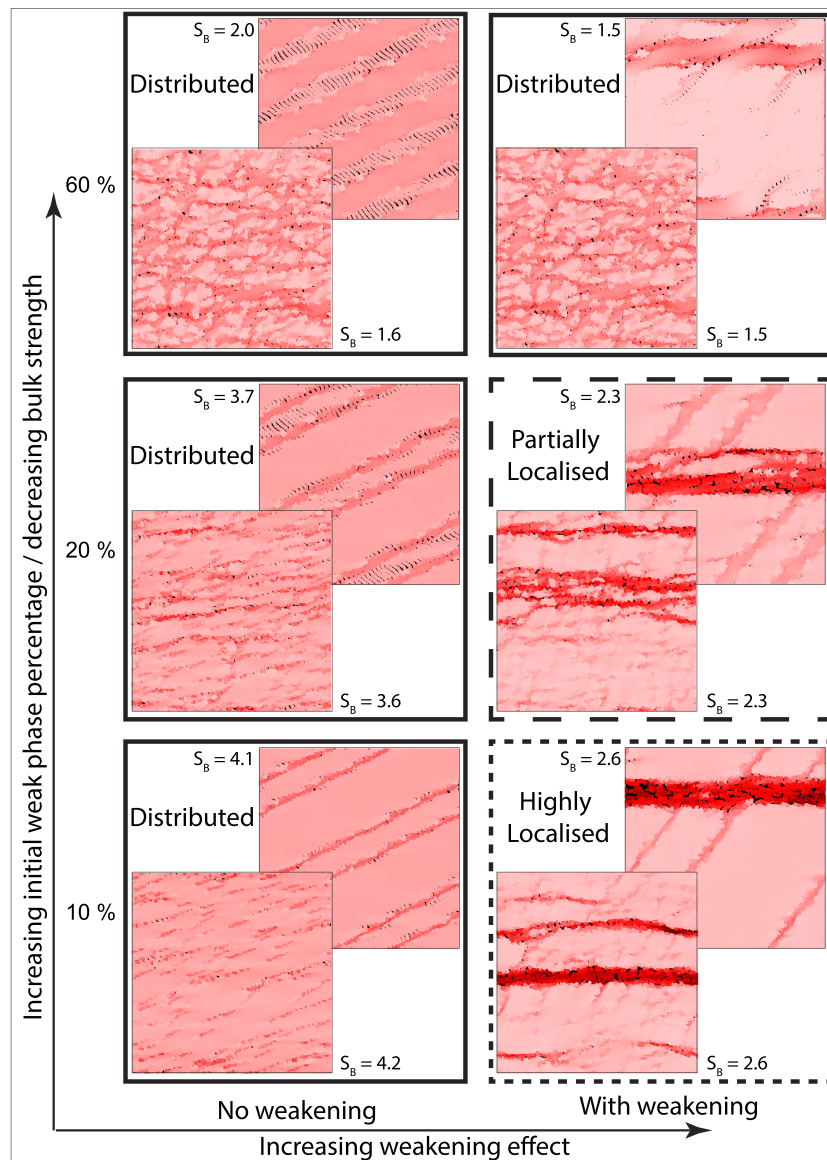


Figure 8. Summary of Regimes I–III: accumulated strain at $\gamma = 2$ showing strain localization as a function of initial weak phase percentage and weakening effect in random (bottom left of each pair) and striped (top right of each pair) geometries. Regime I (solid outline) where strain is distributed; Regime II (dashed outline) where strain is variably distributed, with partial localization; Regime III (dotted outline) where strain is highly localized into HSZ(s).

interconnection of the areas of weak phases is inhibited; hence, Regime I can also form in rheologically strong terrains. A continuous foliation may form in both cases.

The strength of the bulk continental crust is markedly reduced where low levels of partial melt occur (Arzi, 1978; Renner et al., 2000; Rosenberg & Handy, 2005). Experimental evidence also highlights that mica-rich metapelites forming broad schist belts are a very weak component of the continental crust that can accommodate distributed strain within the schist belt without concentrating the strain into HSZs (Mariani et al., 2006; Shea & Kronenberg, 1992). In addition, in extensive areas of clay buried to depths of >5 km, slaty cleavages can be developed causing a marked decrease in strength of the material (Engelder & Marshak, 1985). These field and experimental observations of rheologically weak terrains are largely consistent with our Regime I where materials are characterized by a high weak phase percentage. However, our models show the bulk strength of an area experiencing distributed deformation can be higher than the bulk strength of

an area with a similar proportion of weak phase showing strain localization (compare 10 and 20 area% models in Figure 5b with Figure 5d). Consequently, a pervasive foliation at any scale with or without a cross-cutting HSZ cannot be taken as a clear indicator of a rheologically weak terrain at the time of the foliation development.

Terrains with high proportions of distributed weak phases are expected to exhibit distributed deformation. Here, an SL-IWL or HSZ can form only when the weak phases become stronger, for example, through crystallization of the weak melt phase in high-grade rocks, as they cross the solidus. In contrast, in terrains with low proportions of weak phase, the introduction of any weakening process can initiate strain localization if the process causes weak phase interconnection. Our models suggest this takes effect with as little as ~4% increase in weak phase area. Consequently, we suggest that where a regional foliation is cut by retrograde shear zones, at high-grade conditions the terrain was either (i) rheologically weak due to a high weak phase proportions or (ii) rheologically strong due to a low proportion of weak phase and limited interconnection of the weak phase areas. In the first instance, cooling of the terrain causes the percentage of weak area to be reduced and thus become rheologically hard similar to case (ii). If the weak areas can become interconnected by introducing a syntectonic weakening process, the ongoing deformation can result in localization of the strain. The latter behavior is consistent with our models that show that reducing the weak area percentage, and allowing dynamic weakening will result in the formation of increasingly concentrated HSZs (Figure 8).

Field observations indicate continuous foliations are common in augen gneisses and orthogneisses rather than in metasedimentary sequences which usually display some localization. For example, a mica-rich belt can show distributed strain (Regime I) within the belt, but at the terrain scale, where the belt is surrounded by stronger rocks, the terrain may be experiencing Regime III with strain concentrated into the mica-rich belt. Thus, the scale of observation is important. This correlates with previous modeling showing terrains with weak horizontal layers parallel to the deformation, to be the weakest geometry (e.g., Dell'Angelo & Tullis, 1996) which will readily concentrate any strain (Gardner et al., 2017). In our current modeling the random geometry is able to distribute strain into the dispersed weak phase as there is little interconnection between weak areas, which thereby reduces the likelihood of localizing strain. By contrast, the striped geometry is less able to distribute strain as the weak phase is interconnected in the stripes, allowing formation of SL-IWLs at higher initial proportions of the weak phase. Consequently, layered geological sequences even at high angles to the stress axes tend to favor strain localization if syntectonic weakening is possible.

This study explores the effect of the geometry and weak phase proportion on strain localization. However, these are not the only parameters of importance. For example, Gardner et al. (2017) showed that slight value changes of the weakening threshold caused major changes in model outcomes. Consistent with our results, Hansen et al. (2012) showed that in constant displacement rate analogue experiments, strain localizes only where perturbation in the rheology (e.g., weak phases) occur. However, constant stress boundary conditions readily cause localization into HSZs. Future numerical modeling could investigate the sensitivity of distributed deformation to constant stress boundary conditions and rheological heterogeneity.

5. Conclusions

Our numerical models show that the geometry of the initial weak phase is important in determining which rocks within a terrain readily localize strain. Random geometries can distribute strain without strain localization at higher weak phase percentages compared to layered sequences where the weak phases are intrinsically connected.

Distributed rather than localized deformation (Figure 8, Regime I versus Regime III) is favored if (i) deformation-induced interconnection of the weak phase is inhibited in rocks with low proportions of weak phase or (ii) deformation-induced interconnection of the weak phase is readily possible and/or the initial weak phase area is >60%. In Case (i), strain is localized into both the weak and strong phases and the area is rheologically strong. In Case (ii), strain is localized into only the weak phase causing an SPO to form into only the weak phase, and the area is rheologically weak.

Strain is variably distributed (Figure 8, Regime II) and partially localized if a deformation-induced weakening process causes up to ~10% additional weakening, and high strain develops in ~2% of the area. A more localized HSZ (Figure 8, Regime III) forms where a deformation-induced weakening process causes >

~10% additional weakening and >2% of the area develops high strain. The models also show that HSZs initiate and grow at lower shear strains, are less anastomosing in character, and form with larger increases in weak phase proportion than partially localized SL-IWLs.

Acknowledgments

Logistical and analytical funding was provided by internal funding from the Department of Earth and Planetary Sciences, Macquarie University. Thanks to Jessica Warren as this manuscript is the result of her question at DRT Inverness, UK, May 2017. The authors would also like to thank Susan Ellis, John Platt, and an anonymous reviewer for their careful and constructive reviews, and Thorsten Becker for editorial handling. This is contribution 1385 from the ARC Centre of Excellence for Core to Crust Fluid Systems (<http://www.cafs.mq.edu.au>) and 1332 in the GEMOC Key Centre (<http://www.gemoc.mq.edu.au>). Supporting information is available online at <https://dx.doi.org/10.6084/m9.figshare.10116116>.

References

- Arbaret, L., Burg, J.-P., Zeilinger, G., Chaudhry, N., Hussain, S., & Dawood, H. (2000). Pre-collisional anastomosing shear zones in the Kohistan arc, NW Pakistan. *Geological Society, London, Special Publications*, 170(1), 295–311. <http://sp.lyellcollection.org/content/170/1/295.abstract>
- Arzi, A. A. (1978). Critical phenomena in the rheology of partially melted rocks. *Tectonophysics*, 44(1), 173–184. <http://www.sciencedirect.com/science/article/pii/0040195178900690>
- Bak, J., Korstgård, J., & Sørensen, K. (1975). A major shear zone within the Nagssugtoqidian of West Greenland. *Tectonophysics*, 27(3), 191–209. <http://www.sciencedirect.com/science/article/pii/0040195175900165>
- Barnhoorn, A., Bystricky, M., Kunze, K., Burlini, L., & Burg, J.-P. (2005). Strain localisation in biminerale rocks: Experimental deformation of synthetic calcite-anhydrite aggregates. *Earth and Planetary Science Letters*, 240(3–4), 748–763. <http://www.sciencedirect.com/science/article/pii/S0012821X05005893>
- Beach, A. (1976). The Interrelations of Fluid Transport, Deformation, Geochemistry and heat flow in early Proterozoic shear zones in the Lewisian Complex. *Philosophical Transactions of the Royal Society of London. Series A, Mathematical and Physical Sciences*, 280(1298), 569–604. <http://www.jstor.org/stable/74579>
- Bons, P. D., Koehn, D., & Jessell, M. W. (2008). In P. D. Bons, D. Koehn, & M. W. Jessell (Eds.), *Microdynamics modelling. Lecture notes in Earth sciences* (Vol. 106). Berlin: Springer.
- Brodie, K. H., & Rutter, E. H. (1987). The role of transiently fine-grained reaction products in syntectonic metamorphism: natural and experimental examples. *Canadian Journal of Earth Sciences*, 24(3), 556–564. <https://doi.org/10.1139/e87-054>
- Cao, S., Neubauer, F., Liu, J., Bernroider, M., Cheng, X., Li, J., et al. (2017). Rheological weakening of high-grade mylonites during low-temperature retrogression: The exhumed continental Ailao Shan-Red River fault zone, SE Asia. *Journal of Asian Earth Sciences*, 139, 40–60. <http://www.sciencedirect.com/science/article/pii/S1367912016303030>
- Carreras, J., Czeck, D. M., Druguet, E., & Hudleston, P. J. (2010). Structure and development of an anastomosing network of ductile shear zones. *Journal of Structural Geology*, 32(5), 656–666. <http://www.sciencedirect.com/science/article/pii/S0191814110000477>
- Clarke, G. L., Klepeis, K. A., & Daczko, N. R. (2000). Cretaceous high-P granulites at Milford Sound, New Zealand: Metamorphic history and emplacement in a convergent margin setting. *Journal of Metamorphic Geology*, 18(4), 359–374. <https://doi.org/10.1046/j.1525-1314.2000.00259.x>
- Cook, A. C., Vel, S. S., Gerbi, C., & Johnson, S. E. (2014). Computational analysis of nonlinear creep of polyphase aggregates: Influence of phase morphology. *Journal of Geophysical Research: Solid Earth*, 119, 6877–6906. <https://doi.org/10.1002/2014JB011197>
- Cross, A. J., Ellis, S., & Prior, D. J. (2015). A phenomenological numerical approach for investigating grain size evolution in ductilely deforming rocks. *Journal of Structural Geology*, 76, 22–34. <http://www.sciencedirect.com/science/article/pii/S0191814115000887>
- Davis, B. K., & Forde, A. (1994). Regional slaty cleavage formation and fold axis rotation by re-use and reactivation of pre-existing foliations: The Fiery Creek Slate Belt, North Queensland. *Tectonophysics*, 230(3), 161–179. <http://www.sciencedirect.com/science/article/pii/0040195194901333>
- Dell'Angelo, L. N., & Tullis, J. (1996). Textural and mechanical evolution with progressive strain in experimentally deformed aplites. *Tectonophysics*, 256(1), 57–82. <http://www.sciencedirect.com/science/article/pii/0040195195001662>
- Engelder, T., & Marshak, S. (1985). Disjunctive cleavage formed at shallow depths in sedimentary rocks. *Journal of Structural Geology*, 7(3), 327–343. <http://www.sciencedirect.com/science/article/pii/0191814185900392>
- Frederiksen, S., & Braun, J. (2001). Numerical modelling of strain localisation during extension of the continental lithosphere. *Earth and Planetary Science Letters*, 188(1), 241–251. <http://www.sciencedirect.com/science/article/pii/S0012821X01003235>
- Gardner, R., Piazzolo, S., Evans, L., & Daczko, N. (2017). Patterns of strain localization in heterogeneous, polycrystalline rocks—A numerical perspective. *Earth and Planetary Science Letters*, 463, 253–265. <http://www.sciencedirect.com/science/article/pii/S0012821X17300511>
- Gerbi, C., Johnson, S. E., Cook, A., & Vel, S. S. (2015). Effect of phase morphology on bulk strength for power-law materials. *Geophysical Journal International*, 200, 374–389. <http://gji.oxfordjournals.org/content/200/1/374.abstract>
- Gerbi, C., Johnson, S. E., Shulman, D., & Klepeis, K. (2016). Influence of microscale weak zones on bulk strength. *Geochemistry, Geophysics, Geosystems*, 17, 4064–4077. <https://doi.org/10.1002/2016GC006551>
- Gueydan, F., Précigout, J., & Montési, L. G. J. (2014). Strain weakening enables continental plate tectonics. *Tectonophysics*, 631, 189–196. <http://www.sciencedirect.com/science/article/pii/S0040195114000924>
- Handy, M. R. (1994). Flow laws for rocks containing two non-linear viscous phases: A phenomenological approach. *Journal of Structural Geology*, 16(3), 287–301. <http://www.sciencedirect.com/science/article/pii/0191814194900353>
- Herwegh, M., Poulet, T., Karrech, A., & Regenauer-Lieb, K. (2014). From transient to steady state deformation and grain size: A thermodynamic approach using elasto-visco-plastic numerical modeling. *Journal of Geophysical Research: Solid Earth*, 119, 900–918. <https://doi.org/10.1002/2013JB010701>
- Hobbs, B. E., Mühlhaus, H.-B., & Ord, A. (1990). Instability, softening and localization of deformation. *Geological Society, London, Special Publications*, 54(1), 143–165. <http://sp.lyellcollection.org/content/specpubgl/54/1/143.full.pdf>
- Holyoke, C. W. III, & Tullis, J. (2006). Mechanisms of weak phase interconnection and the effects of phase strength contrast on fabric development. *Journal of Structural Geology*, 28(4), 621–640. <http://www.sciencedirect.com/science/article/pii/S0191814106000241>
- Houseman, G. A., Barr, T. D., & Evans, L. (2008). Basil: Stress and deformation in a viscous material. In P. D. Bons, D. Koehn, & M. W. Jessell (Eds.), *Microdynamics simulation. Lecture notes in Earth sciences* (Vol. 106, Chap. 3.8, pp. 139–154). Berlin: Springer.
- Jessell, M. W., Bons, P. D., Griera, A., Evans, L. A., & Wilson, C. J. L. (2009). A tale of two viscosities. *Journal of Structural Geology*, 31(7), 719–736. <http://www.sciencedirect.com/science/article/pii/S0191814109000868>
- Jessell, M. W., Siebert, E., Bons, P. D., Evans, L., & Piazzolo, S. (2005). A new type of numerical experiment on the spatial and temporal patterns of localization of deformation in a material with a coupling of grain size and rheology. *Earth and Planetary Science Letters*, 239(3–4), 309–326. <http://www.sciencedirect.com/science/article/pii/S0012821X05005443>

- Jiang, D., & Williams, P. F. (1998). High-strain zones: A unified model. *Journal of Structural Geology*, 20(8), 1105–1120. <http://www.sciencedirect.com/science/article/pii/S019181419800025X>
- Leitch, E. C. (1978). Structural succession in a late palaeozoic slate belt and its tectonic significance. *Tectonophysics*, 47(3), 311–323. <http://www.sciencedirect.com/science/article/pii/0040195178900367>
- Mancktelow, N. S. (2002). Finite-element modelling of shear zone development in viscoelastic materials and its implications for localisation of partial melting. *Journal of Structural Geology*, 24(6–7), 1045–1053. <http://www.sciencedirect.com/science/article/pii/S0191814101000906>
- Mariani, E., Brodie, K. H., & Rutter, E. H. (2006). Experimental deformation of muscovite shear zones at high temperatures under hydrothermal conditions and the strength of phyllosilicate-bearing faults in nature. *Journal of Structural Geology*, 28(9), 1569–1587. <http://www.sciencedirect.com/science/article/pii/S0191814106001568>
- Menegon, L., Fousseis, F., Stünitz, H., & Xiao, X. (2015). Creep cavitation bands control porosity and fluid flow in lower crustal shear zones. *Geology*, 43(3), 227–230. <http://geology.gsapubs.org/content/43/3/227.abstract>
- Oliot, E., Goncalves, P., & Marquer, D. (2010). Role of plagioclase and reaction softening in a metagranite shear zone at mid-crustal conditions (Gotthard Massif, Swiss Central Alps). *Journal of Metamorphic Geology*, 28(8), 849–871. <http://simsrad.net.ocs.mq.edu.au/login?url=http://search.ebscohost.com/login.aspx?direct=true&db=aph&AN=53322970&site=ehost-live>
- Oliot, E., Goncalves, P., Schulmann, K., Marquer, D., & Lexa, O. (2014). Mid-crustal shear zone formation in granitic rocks: Constraints from quantitative textural and crystallographic preferred orientations analyses. *Tectonophysics*, 612–613, 63–80. <http://www.sciencedirect.com/science/article/pii/S0040195113006975>
- Piazolo, S., Bons, P. D., Griera, A., Llorens, M. G., Gomez-Rivas, E., Koehn, D., et al. (2018). A review of numerical modelling of the dynamics of microstructural development in rocks and ice: Past, present and future. *Journal of Structural Geology*. <http://www.sciencedirect.com/science/article/pii/S0191814118303067>
- Poirier, J. P. (1980). Shear localization and shear instability in materials in the ductile field. *Journal of Structural Geology*, 2(1), 135–142. <http://www.sciencedirect.com/science/article/pii/0191814180900437>
- Ramsay, J. G. (1980). Shear zone geometry: A review. *Journal of Structural Geology*, 2(1–2), 83–99. <http://www.sciencedirect.com/science/article/pii/0191814180900383>
- Ramsay, J. G., & Graham, R. H. (1970). Strain variation in shear belts. *Canadian Journal of Earth Sciences*, 7(3), 786–813. <https://doi.org/10.1139/e70-078>
- Renner, J., Evans, B., & Hirth, G. (2000). On the rheologically critical melt fraction. *Earth and Planetary Science Letters*, 181(4), 585–594. <http://www.sciencedirect.com/science/article/pii/S0012821X00002223>
- Rosenberg, C. L., & Handy, M. R. (2005). Experimental deformation of partially melted granite revisited: Implications for the continental crust. *Journal of Metamorphic Geology*, 23(1), 19–28. <https://doi.org/10.1111/j.1525-1314.2005.00555.x>
- Rutland, R. W. R., & Etheridge, M. A. (1975). Two high grade schistositys at broken hill and their relation to major and minor structures. *Journal of the Geological Society of Australia*, 22(3), 259–274. <https://doi.org/10.1080/00167617508728896>
- Shea, W. T., & Kronenberg, A. K. (1992). Rheology and deformation mechanisms of an isotropic mica schist. *Journal of Geophysical Research*, 97(B11), 15201–15237. <https://agupubs.onlinelibrary.wiley.com/doi/abs/10.1029/92JB00620>
- Shea, W. T., & Kronenberg, A. K. (1993). Strength and anisotropy of foliated rocks with varied mica contents. *Journal of Structural Geology*, 15(9), 1097–1121. <http://www.sciencedirect.com/science/article/pii/0191814193901587>
- Sibson, R. H. (1977). Fault rocks and fault mechanisms. *Journal of the Geological Society*, 133(3), 191–213. <http://jgs.lyellcollection.org/content/133/3/191.abstract>
- Skemer, P., Warren, J. M., Hansen, L. N., Hirth, G., & Kelemen, P. B. (2013). The influence of water and LPO on the initiation and evolution of mantle shear zones. *Earth and Planetary Science Letters*, 375(0), 222–233. <http://www.sciencedirect.com/science/article/pii/S0012821X13002793>
- Smith, J., Piazolo, S., Daczko, N., & Evans, L. (2015). The effect of pre-tectonic reaction and annealing extent on behaviour during subsequent deformation: Insights from paired shear zones in the lower crust of Fiordland, New Zealand. *Journal of Metamorphic Geology*, 33, 557–670.
- Svahnberg, H., & Piazolo, S. (2010). The initiation of strain localisation in plagioclase-rich rocks: Insights from detailed microstructural analyses. *Journal of Structural Geology*, 32(10), 1404–1416. <http://www.sciencedirect.com/science/article/pii/S0191814110001033>
- Watts, M. J., & Williams, G. D. (1983). Strain geometry, microstructure and mineral chemistry in metagabbro shear zones: A study of softening mechanisms during progressive mylonitization. *Journal of Structural Geology*, 5(5), 507–517. <http://www.sciencedirect.com/science/article/pii/0191814183900561>
- White, S. H., Burrows, S. E., Carreras, J., Shaw, N. D., & Humphreys, F. J. (1980). On mylonites in ductile shear zones. *Journal of Structural Geology*, 2(1), 175–187. <http://www.sciencedirect.com/science/article/pii/0191814180900486>
- Williams, P. F. (1976). Relationships between axial-plane foliations and strain. *Tectonophysics*, 30(3), 181–196. <http://www.sciencedirect.com/science/article/pii/0040195176901864>
- Zheng, G., Wang, H., Wright, T. J., Lou, Y., Zhang, R., Zhang, W., et al. (2017). Crustal deformation in the India-Eurasia collision zone from 25 years of GPS measurements. *Journal of Geophysical Research: Solid Earth*, 122, 9290–9312. <https://agupubs.onlinelibrary.wiley.com/doi/abs/10.1002/2017JB014465>